

OSCILLATORY FAILURE DETECTION IN AIRCRAFT ACTUATION SYSTEMS USING WAVELET TRANSFORM

Isabella Ono Skusa[12], Raphael das Neves Calvo[2] & Alberto Adade Filho[1]

[1]ITA, Instituto Tecnológico de Aeronáutica, São José dos Campos, Brazil
[2]Embraer, São José dos Campos, Brazil

Abstract

This article addresses the issue of early Oscillatory Failure Cases (OFCs) detection in aircraft flight control systems. OFCs are characterized by sustained undamped oscillations in flight control surfaces, typically within the 0.1–10 Hz frequency range. Detecting these failures within three cycles is critical to ensure aircraft safety and structural integrity; otherwise, structural reinforcement may be required, increasing aircraft weight. This work investigates the use of Wavelet Transforms in the design of analytical redundancy-based monitors for detection of OFCs.

The monitoring system was evaluated using simulated faults affecting the piston Linear Variable Differential Transformer (LVDT) of an active-active flight control actuator. This work focuses on the selection of the observer architecture and wavelet parameters required to satisfy the three-cycle detection requirement. The final design combines a closed-loop Luenberger observer with DWT-based residual analysis. The observer uses piston position, servo-valve spool position, and chamber pressure differential as feedback signals, while a Daubechies order-3 wavelet is applied to the resulting residual.

Simulation results show that the proposed monitor successfully detects the studied faults within three cycles of fault onset.

Keywords: Oscillatory Failure Case, LVDT, fault detection, wavelet transform, Luenberger observer, flight control system.

1. Introduction

Fly-By-Wire (FBW) technology introduced a new flight control architecture based on fault-tolerant computers, sensors, digital databuses, and electrohydraulic servo-actuators. This architecture provides enhanced control performance, reduced pilot workload, and flight envelope protection. However, its increased complexity also introduced new failure modes. These failures must be detected and mitigated promptly to prevent the development of safety-critical conditions.

A particularly relevant failure category in this context is the Oscillatory Failure Case (OFC), in which a fault in the actuation loop forces a sustained undamped oscillation on a primary control surface. If the OFC cannot be detected and addressed promptly, there must be a reinforcement of the structure to account for these additional loads, leading to an increase in aircraft weight. Therefore, early and robust fault detection methods are essential and intrinsic to Fly-By-Wire systems to ensure the integrity of passengers, crew, cargo and the aircraft itself. [1]. Figure 1 shows the typical sources of OFCs inside the actuator control loop, including the actuator position sensor, the surface sensor and their analog-to-digital conditioning, the command current sent to the servo-valve, and mechanical faults in the electro-hydraulic servo-valve itself.

In the literature, a well-known application of OFC detection in FCS is the Airbus A380 OFC detection architecture described by Goupil [3], where residuals generated through parity equations are filtered and evaluated using oscillation counting methods. Subsequent works improved residual generation through nonlinear modeling and observer-based architectures that attenuate disturbances and

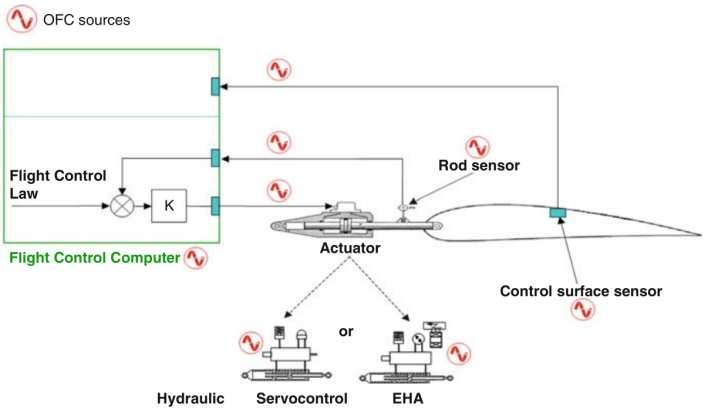


Figure 1 – OFC sources inside the actuator control loop. Source: [2].

reduce residual noise [4, 1]. Alternative residual evaluation strategies, including Fourier-based methods, adaptive thresholds and wavelet decomposition, have also been explored [5, 6, 7, 8, 9]. Two gaps of this body of work motivate the present article. First, most studies concentrate on residual generation, leaving residual evaluation comparatively underexplored. Second, most studies target the active-damped actuator architecture used in the A380, while results on the active-active architecture remain scarce.

Additionally, in the literature of signal processing for fault detection methods, wavelet transforms have attracted significant attention due to their advantages for analysis of non-stationary and transient phenomena [10]. Similarly to Fourier transforms, wavelets are convolutions of a function with the signal, but instead of sines and cosines, they are convolutions with wavelets – a waveform of limited duration.This characteristic makes wavelets particularly suitable for fault detection problems involving abrupt changes or oscillatory behaviors that vary over time. Applications of wavelet-based fault diagnosis have been extensively explored in areas such as power transmission systems and rotating machinery [11, 12, 13, 14, 15].

This article addresses these literature gaps by developing an OFC detection method based on wavelet analysis of analytical redundancy residuals. The proposed approach is developed and assessed in an active-active flight control system, a configuration that remains less explored in the literature than active-standby architectures.

The development of the proposed monitor follows three main steps. First, electrical and mechanical LVDT faults are simulated within the flight control system model, and their effects on the control surface response are characterized. To identify which of these fault scenarios are capable of producing hazardous oscillations, the resulting surface responses are evaluated against a generalized oscillation envelope. This envelope defines acceptable control surface oscillation amplitudes as a function of frequency and was selected as a representative of typical oscillation limits encountered in aircraft flight control systems. The identified scenarios are then used to assess the detection capability of a sum-voltage monitor commonly implemented in LVDTs and to determine the remaining detection gaps. Second, different observer architectures are evaluated, leading to the selection of a closed-loop Luenberger observer capable of generating a residual sensitive to LVDT faults. Finally, a wavelet-based detection layer is designed, including the selection of mother wavelet, implementation method, sampling strategy, buffer configuration, and detection thresholds required to meet the OFC detection requirements.

The remainder of the article is organized as follows. Section 2. summarizes the wavelet transform background needed to follow the design. Section 3. describes the system model, the LVDT and the fault scenarios. Section 4. characterizes the surface response and identifies the detection gaps. Section 5. presents the proposed observer and the wavelet residual evaluation. Section 6. reports the simulation results, and Section 7. concludes.

2. Wavelet Transform Background

A detailed mathematical treatment of wavelet theory can be found in [16]. This section presents only the concepts necessary to understand the methodology proposed in this work.

2.1 Multiresolution Analysis

The detection of oscillatory faults requires identifying not only which frequency components are present in a signal, but also when they occur. Classical frequency-domain analysis based on the Fourier Transform (FT) provides spectral information but lacks temporal localization. The Short-Time Fourier Transform (STFT) partially addresses this limitation through windowing, although it remains constrained by a fixed time-frequency resolution trade-off. Wavelet transforms overcome this limitation through multiresolution analysis, employing short windows at high frequencies and long windows at low frequencies, which makes them particularly suitable for the analysis of transient and oscillatory phenomena.

Despite this advantage, wavelet transforms remain constrained by the Heisenberg uncertainty principle,

$$\sigma_t \sigma_f \geq \frac{1}{4\pi}, \tag{1}$$

where σ_t and σ_f denote the spreads in time and frequency, respectively. Therefore, improving temporal localization necessarily worsens frequency localization, and vice versa. A wavelet compressed in time occupies a broader frequency band, whereas a stretched wavelet provides finer frequency resolution at the expense of temporal localization.

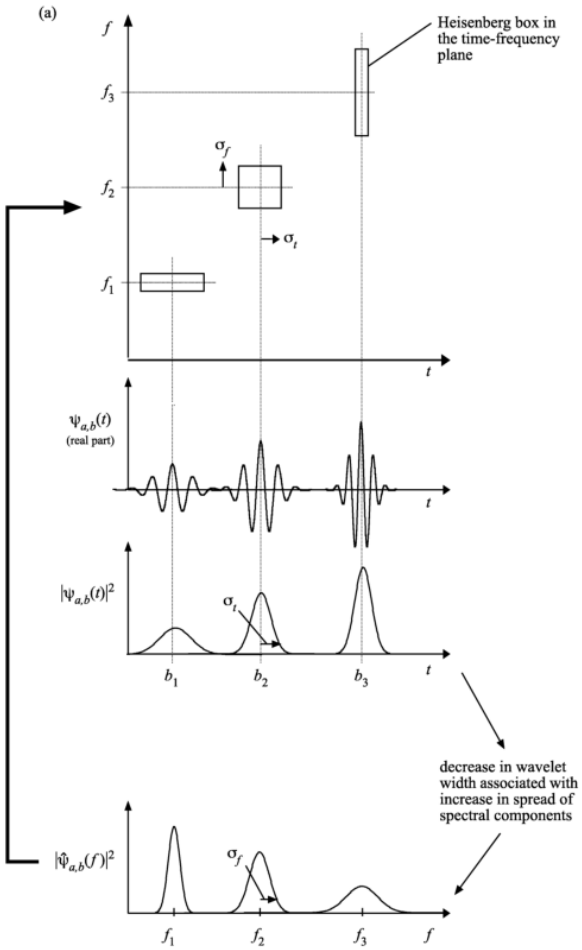


Figure 2 – Illustration of the Heisenberg principle for scaled wavelets. Source: [16].

Figure 2 illustrates this trade-off across different wavelet scales. At high frequencies, the wavelet becomes narrow in time and broad in frequency, whereas at low frequencies it becomes broader in

time and narrower in frequency. This adaptive resolution is one of the main advantages of wavelet analysis for oscillatory fault detection.

2.2 Wavelets

Wavelet analysis is based on a mother wavelet $\psi(t)$, whose scaled and translated versions form a family of finite-duration, zero-mean waveforms. The choice of mother wavelet depends on the characteristics of the analyzed signal and the objectives of the application. For oscillatory fault detection, the time-frequency localization properties of the selected wavelet will either emphasize the monitor capacity to isolate frequencies or its capacity for fast and accurate detection.
A wavelet characteristic directly related to time-frequency localization is its support. The support of a wavelet corresponds to the time interval over which the wavelet assumes non-zero values. In general, wavelets with shorter support provide better temporal localization, whereas wavelets with longer support provide improved frequency selectivity. Consequently, different mother wavelets exhibit different trade-offs between time and frequency resolution.

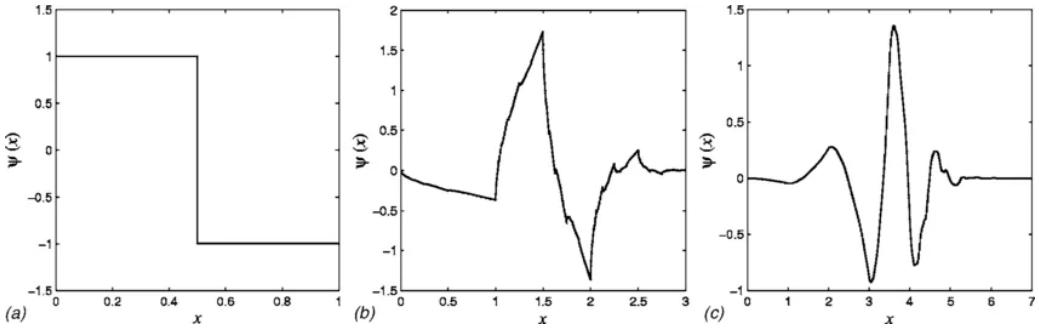


Figure 3 – Daubechies Wavelets shown over their respective supports. (a)db1 or Haar Wavelet, (b) db2, (c) db3. Source: [17].

The Haar wavelet has the shortest support and excellent temporal localization, making it suitable for detecting abrupt changes and transient events. However, its frequency selectivity is limited. Daubechies wavelets offer a compromise between extremes and are widely used in engineering applications. Figure 3 illustrates the increase in order in Daubechies Wavelets. Increasing the Daubechies order increases the support length and smoothness of the wavelet, improving frequency selectivity while reducing temporal localization. The wavelet adopted in this work is discussed in Section 5.2.

2.3 Continuous and Discrete Wavelet Transforms

Given a mother wavelet $\psi(t)$, the Continuous Wavelet Transform (CWT) of a signal $x(t)$ is defined as

$$CWT(a,b) = \frac{1}{\sqrt{|a|}} \int_{-\infty}^{\infty} x(t)\psi^* \left(\frac{t-b}{a} \right) dt, \tag{2}$$

where a is the scale parameter and b is the translation parameter.
By scaling and translating this function, as shown in figure 4 a family of wavelets is generated to analyze different frequency ranges and time locations within a signal.
The scaling parameter controls the wavelet frequency content: small scales correspond to compressed wavelets associated with high frequencies, whereas large scales correspond to stretched wavelets associated with low frequencies. The translation parameter determines the wavelet position in time. The mother wavelet must satisfy admissibility conditions detailed in [16].
The CWT provides a detailed time-scale representation of the signal but is computationally expensive and highly redundant because it evaluates many combinations of scales and translations. For practical implementations, the Discrete Wavelet Transform (DWT) is generally preferred. The DWT discretizes scales and translations, typically using dyadic sampling, which significantly reduces computational complexity while preserving the essential time-frequency information.



Figure 4 – Effects of the scale and translation parameter over the mother wavelet. (a) Wavelet translations, (b) Wavelet Scaling. Source: Adapted from [16].

An efficient implementation of the DWT is obtained through cascaded filter banks. At each decomposition level, the signal is processed by a low-pass filter, producing approximation coefficients that represent the low-frequency content, and by a high-pass filter, producing detail coefficients that capture high-frequency components. The outputs are then downsampled by a factor of two, and only the approximation coefficients are further decomposed. This recursive structure is illustrated in Figure 5.

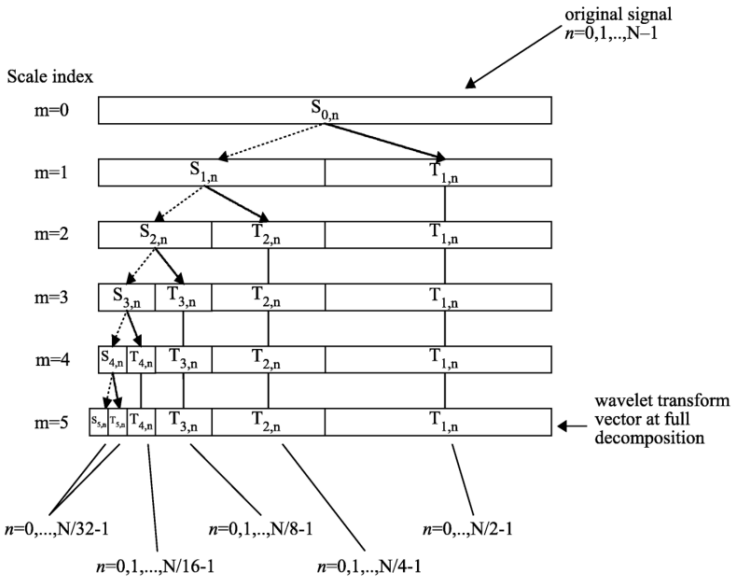


Figure 5 – Filter-bank implementation of the DWT. Source: [16].

Due to its reduced computational cost, non-redundant representation, and efficient filter-bank implementation, the DWT is widely employed in real-time signal processing applications, including denoising, compression, and fault detection systems. These characteristics make it particularly suitable for the real-time oscillatory fault monitor proposed in this work.

3. System Model and LVDT Fault Modes

3.1 Actuation system

Existing models from previous researches ([18] and [19]) were adapted in order to construct a flight control system with dual active-active actuators. Figure 6 shows the physical system modeled in Simulink. The model works with a command input for surface movement and simulates up to the surface displacement, including aerodynamic forces, controller with sensor dynamics, servo valve, piston rod, cylinder and surface dynamics.

Figure 7 shows the baseline response to a 30-degree step command without fault, with the surface subjected to aerodynamic loads. The plot includes the surface position, the piston position X_p, the servo-valve spool position X_v and the pressure differential between cylinder chambers ΔP.

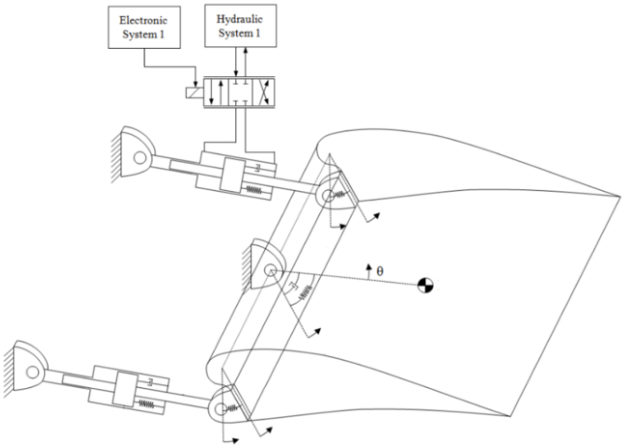


Figure 6 – Schematics of the simulated active-active actuation system. Adapted from [18].

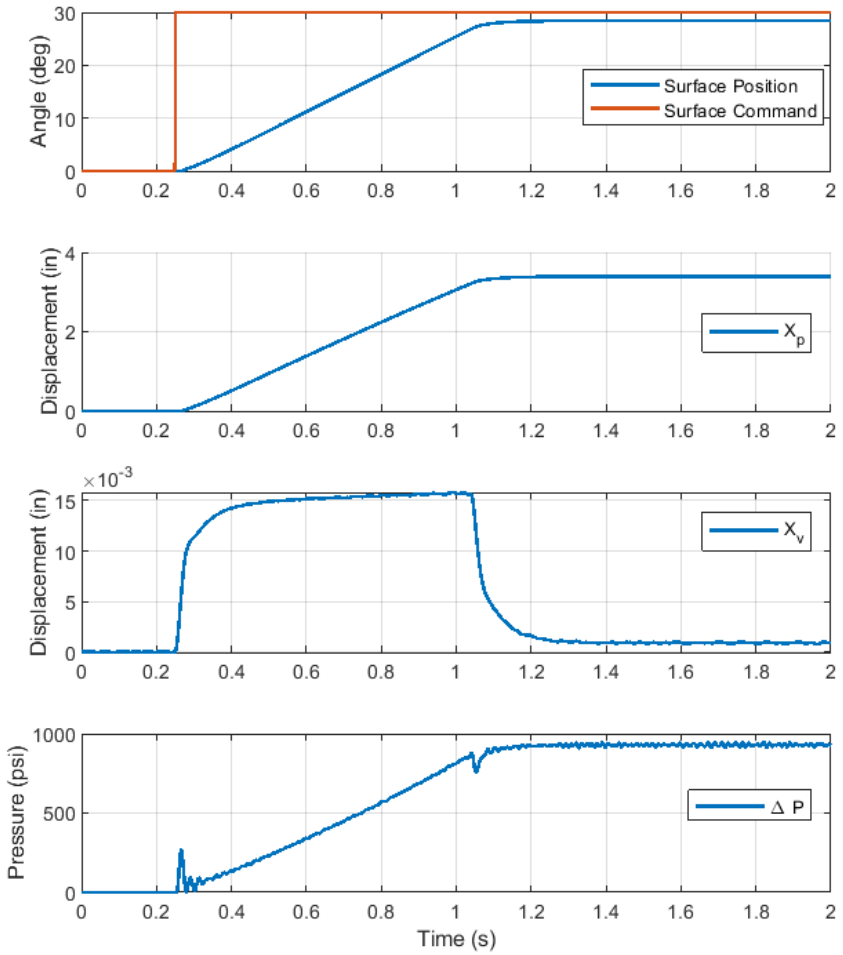


Figure 7 – Baseline system response to a 30-degree step command, no fault.

3.2 LVDT modeling

The piston position is measured by a Linear Variable Differential Transformer (LVDT), an electromechanical transducer that converts linear displacement into an electrical signal. An LVDT consists of three coaxial solenoidal windings on a hollow cylinder: a primary winding and two identical secondary windings symmetrically placed on either side. A movable ferromagnetic core slides within the cylin-

der, modulating the magnetic coupling between the coils as it moves. An AC excitation is applied to the primary; the two secondary coils are wound out of phase, and their voltages are subtracted to form the differential output

$$V_{\text{diff}} = V_{\text{sec1}} - V_{\text{sec2}}. \tag{3}$$

Figure 8 illustrates the principle: when the core is centered, $V_{\text{diff}} = 0$; otherwise the sign and magnitude of V_{diff} reflect the direction and amount of core displacement.

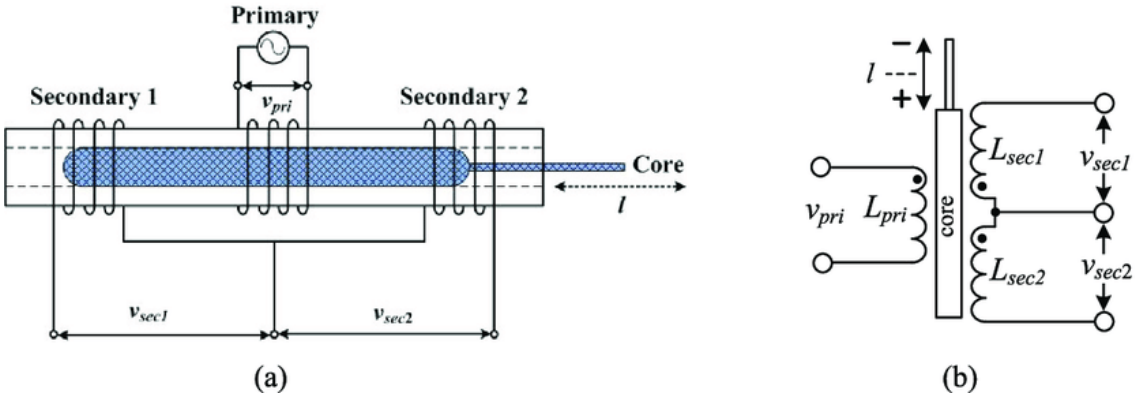


Figure 8 – Schematic of an LVDT showing primary excitation and induced voltages in secondary windings. Source: [20].

For simulation purposes, the LVDT secondary signals are represented by their RMS values, denoted V_a and V_b. With this DC approximation, V_a and V_b vary linearly in opposite directions with the piston displacement x_p, while their sum remains approximately constant at 3.5 V over the entire stroke [19]. The LVDT model used in this work is the same as in [19], extended with electrical and mechanical fault injection paths.

3.3 Baseline monitor: sum-voltage

The constant value of $V_a + V_b$ enables a simple sensor-level integrity monitor that is standard in LVDT installations: the sum-voltage monitor. If $V_a + V_b$ deviates from its nominal value beyond a tolerance, a fault is declared. In this work, the thresholds are set at $\pm 10\%$ around the nominal 3.5 V, that is, 3.15 V and 3.85 V, with a persistence of 30 ms.

3.4 LVDT fault scenarios

Both LVDT fault types considered are introduced as liquid faults: an oscillatory signal of fixed frequency and amplitude is added to the nominal signal rather than substituting it. Solid faults are out of scope.

Electrical fault. The electrical fault models phenomena such as short circuits or electromagnetic interference acting on the LVDT signal conditioning. It is injected by adding an oscillatory signal directly to the RMS voltage V_a. Because V_a is the RMS of an AC voltage and cannot be negative, only positive-valued liquid oscillations are considered, with a maximum amplitude of approximately 1.8 V. The corrupted feedback drives the PID to compensate for an error that does not exist physically, producing an oscillatory command to the servo-valve and a sustained oscillation in the actuator and, through the active-active interaction, in the control surface. Figure 9 shows the system response to a 0.5 Hz, 1.8 V electrical fault under a 10-degree surface command. The piston of actuator 1 moves in phase opposition to the fault, while actuator 2 tracks the reference; the resulting force fight limits the surface motion to approximately 11 degrees.

Mechanical fault. The mechanical fault models non-uniform or unstable motion of the LVDT core inside the cylinder due to wear, internal friction, bending of the rod or contamination by metal debris or hydraulic fluid. It is injected by adding an oscillatory signal directly to x_p inside the LVDT model,

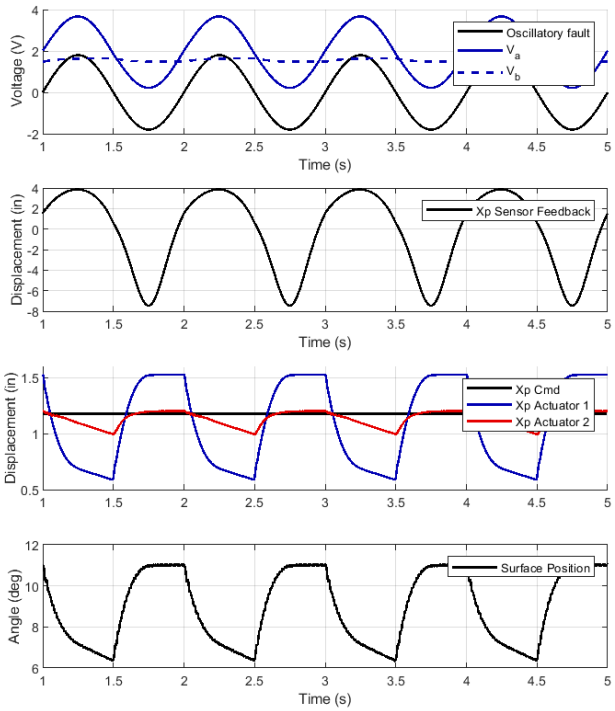


Figure 9 – System response to a 0.5 Hz, 1.8 V OFC in the LVDT electrical part.

before the voltage decomposition. The closed-loop interpretation of these spurious displacements amplifies the perceived motion and produces sustained low-amplitude oscillations in the actuator and surface. Figure 10 shows the response to a 0.7 Hz, 1 in mechanical fault under a 10-degree surface command. The propagation pattern is qualitatively similar to that of the electrical fault.

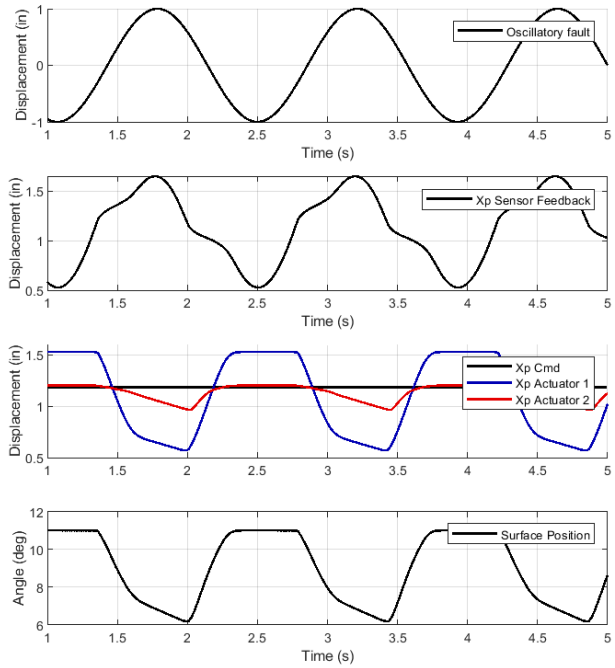


Figure 10 – System response to a 0.7 Hz, 1 in OFC in the LVDT mechanical part.

4. Detection Gaps and Requirements

The acceptable oscillation amplitude of the control surface as a function of frequency is bounded by a reference envelope, shown in Figure 11. Above this envelope, the airframe is exposed to excessive

structural loads.

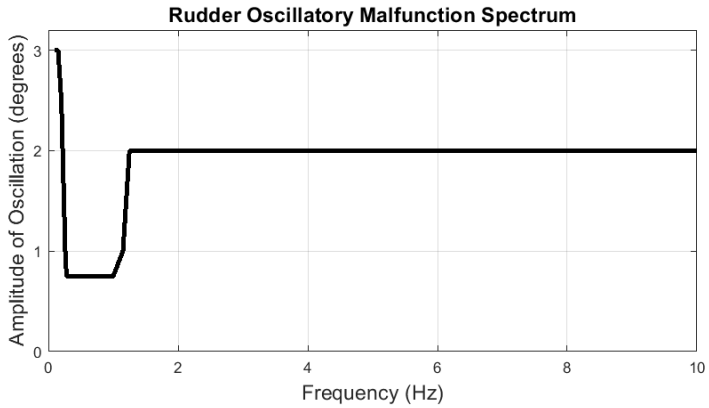


Figure 11 – OFC envelope requirement.

Each combination of fault type, frequency and amplitude was simulated and the resulting surface oscillation amplitude was mapped against the envelope. Figure 12 shows the resulting surface oscillation amplitude and surface oscillation frequency for each fault amplitude. The envelope is also represented as a green line.The values mapped above the green line represent faults in the LVDT that generated oscillations above the acceptable on the control surface.

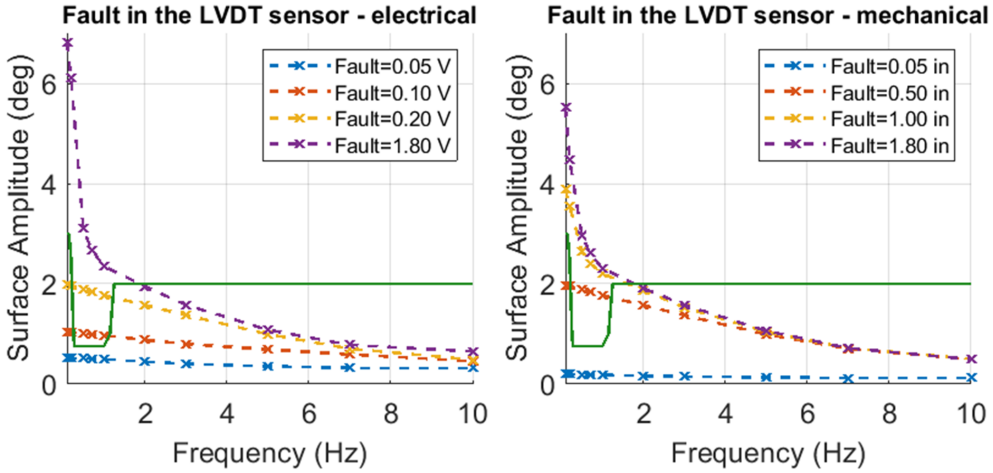


Figure 12 – Surface oscillation amplitude for different LVDT fault amplitudes and frequencies, against the envelope.

Two regions of the envelope deserve attention. First, between 0.3 Hz and 1 Hz, the envelope exhibits a valley: in this band the aircraft is intolerant to small surface oscillations, and small fault amplitudes are sufficient to violate the limit. Second, above 2 Hz the same fault amplitudes produce smaller surface oscillations, and all cases considered fall under the envelope. The frequency range of interest for monitor design is therefore 0.1 to 2 Hz.

Table 1 lists the fault amplitudes located at the envelope limit for each frequency and each fault type. These are the minimum fault amplitudes that must be detected, since any larger amplitude exceeds the envelope. The cells in red represent gaps not covered by the sum-voltage monitor; the cell in green is the only case in which the sum-voltage monitor is sufficient. The electrical fault is detected by the sum-voltage monitor only at 2 Hz, where the required fault amplitude (1.8 V) is large enough to violate the $\pm 10\%$ threshold on $V_a + V_b$. The mechanical fault is not detected by the sum-voltage monitor at any frequency, because it does not perturb the relation $V_a + V_b$. All remaining cases require a dedicated OFC monitor.

Two performance requirements are imposed on the proposed monitor. First, detection must occur within three cycles of fault onset for any frequency in the 0.1 to 2 Hz range, which makes 2 Hz the

Frequency (Hz)	Electrical fault (V)	Mechanical fault (in)
0.1	0.30 (±0.01)	0.77 (±0.01)
0.2	0.25 (±0.01)	0.53 (±0.01)
0.5	0.07 (±0.01)	0.17 (±0.01)
0.7	0.07 (±0.01)	0.18 (±0.01)
1	0.07 (±0.01)	0.19 (±0.01)
2	1.8 (±0.2)	1.8 (±0.2)

Table 1 – Minimum LVDT fault amplitudes that exceed the surface envelope. Red: gaps not covered by the sum-voltage monitor. Green: covered.

timing bottleneck. Second, the monitor must provide an adequate threshold margin between the no-fault and faulty conditions, to keep the false-alarm rate low.

5. Proposed Wavelet-Based Monitor

The proposed monitor relies on analytical redundancy, where a state observer estimates the piston position from the linearized model and generates a residual through comparison with the LVDT measurement. The residual is then evaluated by a wavelet-based detection layer.

5.1 Observer design

Four candidate observer architectures were evaluated, all based on the linearized state-space model from [19]. Figure 13 shows the real system at the top, followed by the four different observer systems tested, that will be described next.

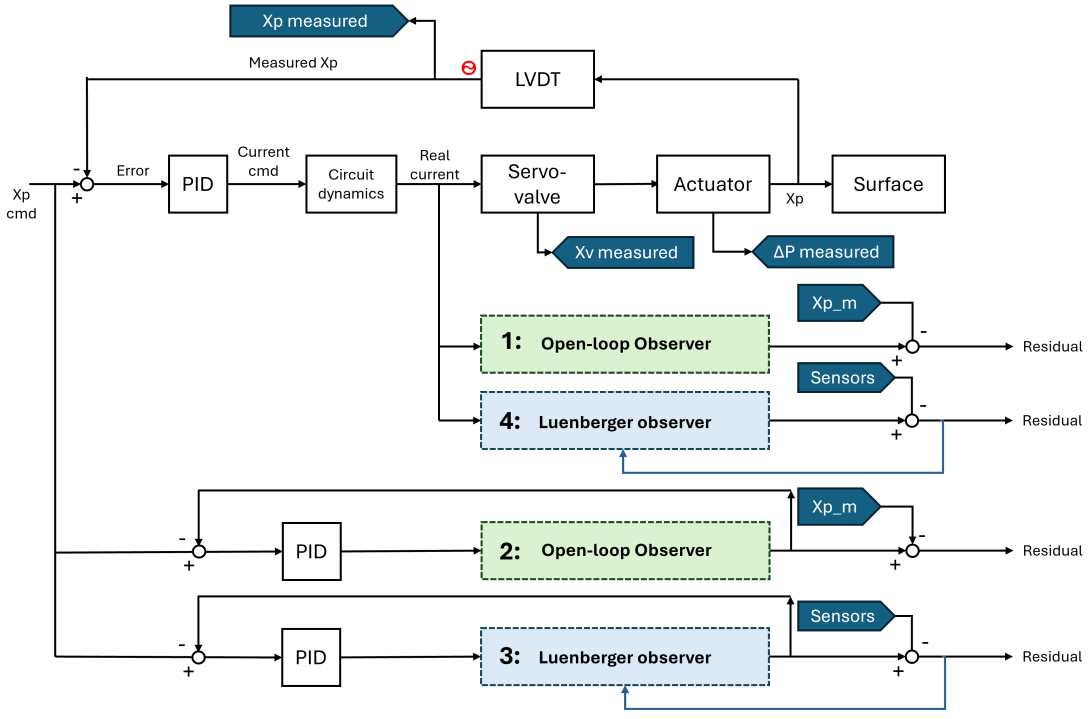


Figure 13 – Real system and candidate observer architectures.

- **Monitor 1 - Open-loop without dedicated PID:** The first observer implemented was an open-loop observer. The input to this observer is the current command that feeds the servo valve. The command current is generated by the PID controller, that processes the error between the desired piston position and the measured piston position.

  However, in the real system, physical losses such as piston leakage and valve leakage require a constant bias current to compensate for these effects. When this bias is applied to the linearized

model, it results in a ramp response due to an integrator pole (a real pole in zero, associated with the piston displacement dynamics), as seen in Figure 14. The figure shows the system subjected to a step input of 10 degrees. The response does not converge to a stable value, which eliminates the effectiveness of this open-loop configuration for fault detection.

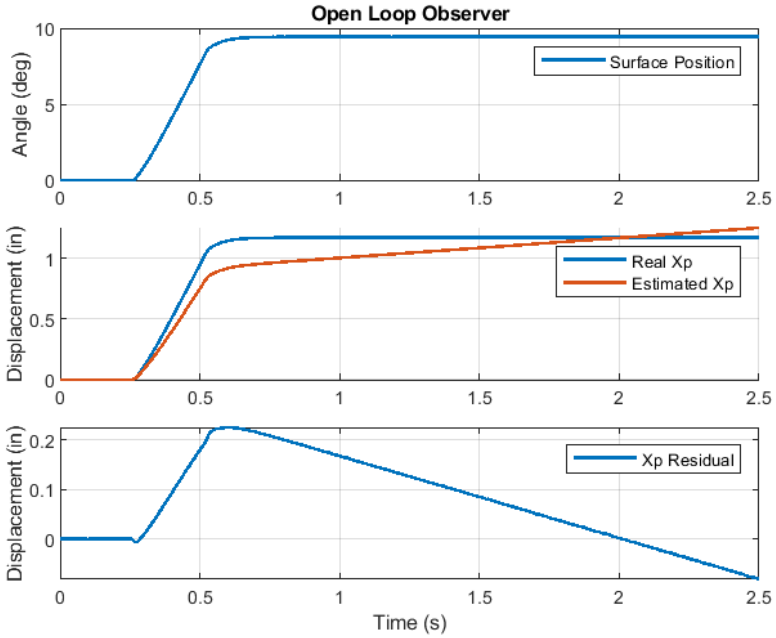


Figure 14 – Open Loop Observer response to a 10 degree step command to the surface position

- **Monitor 2 - Open-loop with dedicated PID:** Since the open-loop observer was not able to reject the estimation error, the next improvement was to implement a duplicated PID controller within the observer. This PID was configured to mirror the one used in the real system, but it operates exclusively on the linear model. In this case, the reference signal, which is originally defined in degrees and converted into piston displacement, was used as the input.

  The estimation error was then computed as the difference between the reference displacement and the observer's estimated X_p. By processing this error, the duplicated PID was able to compensate for the integrator pole effect in the linear model, enabling the observer to converge. Importantly, the observer was no longer relying on the control output of the real system but instead generated its own correction through the duplicated PID, thus improving the overall estimation performance.

  Figure 15 shows the improvement on estimation and a lower residual value.

- **Monitors 3 and 4 - Closed-loop with and without dedicated PID (Luenberger):** To further reduce the residuals under fault-free conditions, a closed-loop Luenberger observer was implemented. Both the closed-loop observer with a dedicated PID and without the PID were implemented and compared. The difference between both residuals was negligible, so the decision was made to use the Luenberger without a dedicated PID, so to use less processing power.

  In order to properly design the closed-loop observer, it was necessary to define adequate observer poles. These poles were chosen to be compatible with a sampling rate of 500 Hz, a common rate for processors in aircraft embedded electronics, while also being as fast as possible to ensure a rapid dynamic response. The poles were placed around 250 Hz, guarantying a good representation by a 500 Hz processor and making the convergence of the estimated value to the measured value faster. Table 2 compares the poles of the linear system to the new poles allocated in the Luenberger observer.

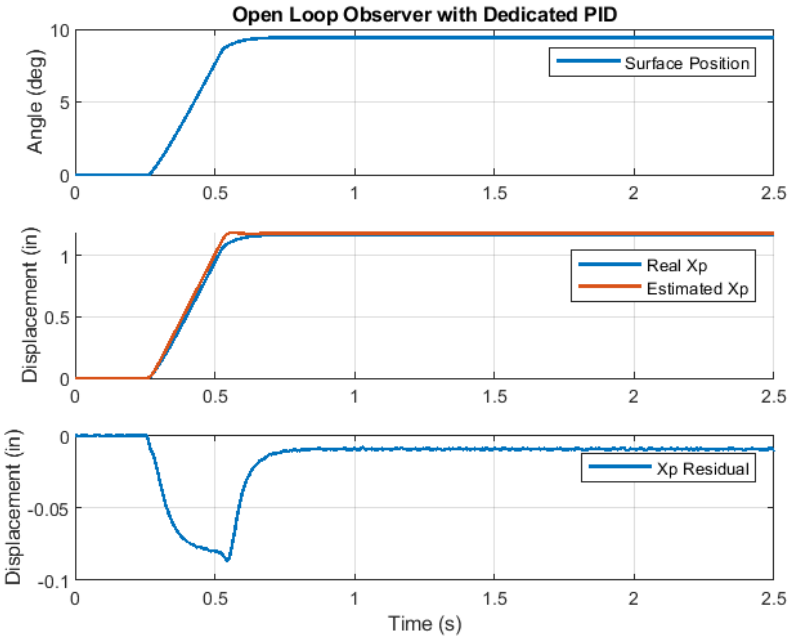


Figure 15 – Open Loop Observer with dedicated PID response to a 10 degree step command to the surface position

Table 2 – Comparison between original poles and Luenberger-assigned poles (placeholders).

Original Poles	Luenberger Poles
$-1343 \pm 4091\,\mathrm{i}$	$-1450 \pm 600\,\mathrm{i}$
-955	-1570
$-23 \pm 458\,\mathrm{i}$	$-1170 \pm 458\,\mathrm{i}$
0	-1260

The first attempt at this configuration relied solely on feedback from the piston displacement sensor (X_p). However, since the oscillatory fault is located inside the LVDT sensor, the faulty signal was the only feedback to the observer. As a consequence, the resulting residuals showed very poor separation between the faulty and fault-free cases. This limitation highlighted the need to rethink the feedback structure by incorporating additional measurements. Consequently, other states that are not directly influenced by the LVDT fault, such as the pressure differential (ΔP) and the servo valve spool position (X_v), were included to improve the robustness and sensitivity of the observer.

Figure 16 is a graphical representation of the time series of internal states of both closed-loop observers, with and without dedicated PID. The graphs on the left illustrates the monitor only with the piston LVDT sensor feedback (the residual was of the magnitude 1e-4), while the right side includes the other sensors as well. It is clear, that including these other sensor's feedback increased the monitor's sensitivity to fault, while increasing the residual's noise.

5.2 DWT-based residual evaluation

The DWT was selected over the CWT because of its lower computational cost and non-redundant representation, which are decisive for an embedded real-time monitor. The DWT was implemented via the filter bank decomposition introduced in Section 2., with sum-of-magnitudes of detail coefficients at the final segment of each level used as the per-level detection metric.

Buffer and sampling. Figure 17 illustrates how the acquisition rate and buffer size were defined for the piston observer wavelet design, aimed at identifying LVDT faults. Since the faults occur over

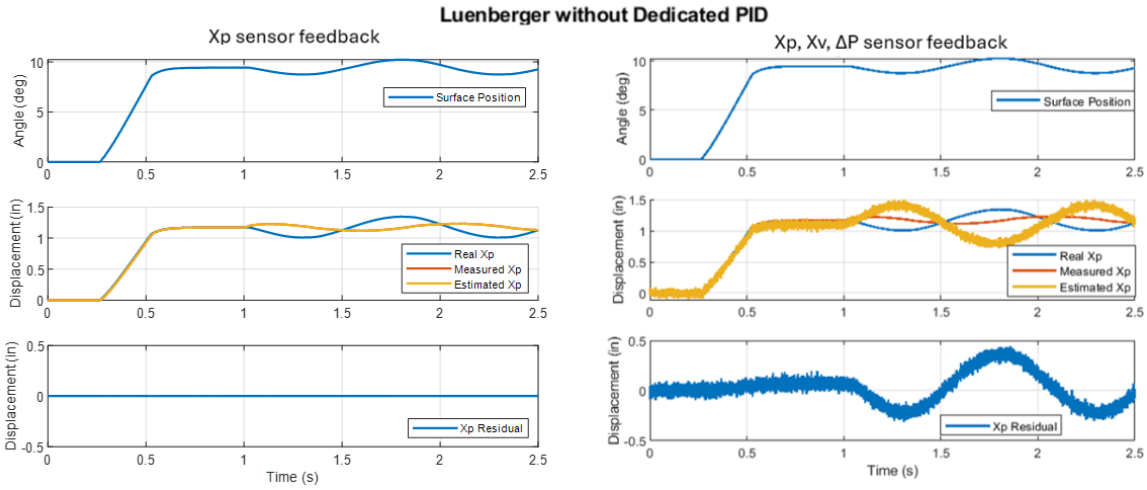


Figure 16 – Comparison between a closed-loop observer with only x_p feedback (left) and with Xp, Xv and ΔP feedback from sensors

a wide frequency range, from 0.1 to 2 Hz, multiple decomposition levels were necessary. Five levels were defined, with level 5 targeting the lowest frequencies between 0.1 and 0.2 Hz, and the highest level covering frequencies from 1.6 to 3.2 Hz. A total of 256 points were selected to ensure that even at the last level a reasonable number of points, specifically 8, remained for analysis. The acquisition rate of 6.4 Hz was chosen to allow the frequencies to be favorably divided, optimizing fault identification.

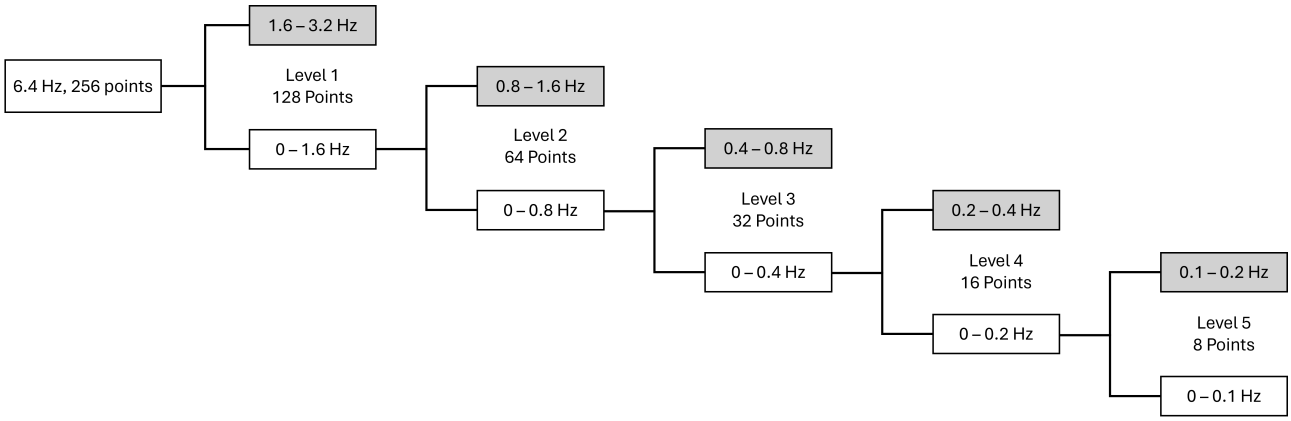


Figure 17 – DWT level characteristics adopted for the piston residual.

The buffer update rate was designed according to the fastest fault, occurring at 2 Hz. Since this fault must be detected within less than three cycles (since there are delays in the system, a conservative two cycles was used for this design), the wavelet analysis needs to process and receive new points from the buffer, at least, every 1 second. In other words, at least one DWT analysis (one buffer update) must be made at every second, to guarantee that a 2 Hz fault will be identified under 2 cycles of it initiating. For security, a DWT analysis was performed each time a sample was taken from the signal, i.e. the buffer update rate was 6.4 Hz.

For each decomposition level, a certain number of final coefficients are available. Since the goal is to evaluate a fault only at around two cycles, the analysis considers the last coefficients in each level, corresponding to the number of points required for two cycles of the fault frequencies within that level. The coefficients are summed up in each level, to estimate a magnitude of signal in the final moments of the time series, for each level. To compare the coefficients magnitude to a threshold, the sum of each level is then summed up again to have a final value for that specific time series, generated by the buffer.

Wavelet choice. The Haar wavelet was tested first because of its strong temporal localization, but its broad frequency response produced significant leakage between levels, generating large coefficients at undesired frequencies. The Daubechies family was then considered, and orders 2 and 3 were compared. The third-order Daubechies (db3, also known as D6) provided the best balance between frequency selectivity and time localization for this application, and was adopted.

Threshold strategy. The surface envelope has a valley between approximately 0.2 Hz and 2 Hz, which means that the maximum allowable fault amplitudes differ significantly between the low-frequency band (0.1 and 0.2 Hz, larger amplitudes allowed) and the higher-frequency band (0.5, 0.7 and 1 Hz, smaller amplitudes allowed). A single threshold over the aggregated coefficients would therefore be too conservative in one band or too permissive in the other. To address this, the per-level sums of detail coefficients are aggregated separately for the low-frequency levels (4 and 5) and for the higher-frequency levels (1, 2 and 3), and a separate threshold is defined for each group.

6. Simulation Results

The proposed monitor was evaluated against the gaps in Table 1, with the fault amplitudes set to the minimum values listed there (the limit of the envelope). All simulations were carried out under nominal operational conditions of the FCS.

The resulting figures illustrate the analysis for the different frequency ranges. Table 3 presents the results for the 0.1 and 0.2 Hz frequencies, while table 4 shows the higher frequency ranges. As the sums were computed separately for these groups, the thresholds used for fault detection were also defined differently for the low- and high-frequency ranges.

In table 3, it can be observed that the threshold is significantly higher, close to 6. This value was chosen as the average between the signal magnitude over approximately two cycles at 0.1 Hz, which corresponds to the lowest-amplitude fault, and the signal at 0.2 Hz, where the amplitudes are considerably larger. As a result, a wide margin can be seen in this case, particularly for this observer.

The residual signals exhibited a considerable amount of noise, mainly due to the pressure sensor, which introduced significant high-frequency components into the observer. As a result, the no-fault piston displacement residual (X_p) reached amplitudes around 0.3. On table 4, the magnitude of the coefficients is noticeably smaller, with the residual itself reaching only about 0.4. This reduction is again related to the envelope of allowable amplitudes, which is much narrower in this frequency range. Even so, the wavelet analysis, was effective in filtering out these high-frequency disturbances, yielding a clear separation between the faulty and no-fault cases.

In this case, the threshold ended with a margin of around 100% over the no-fault coefficient value, validating the feasibility of a wavelet implementation. Even with the improvement, the magnitude differences remains relatively small, meaning that the detection margin was not very large. Even so, the results demonstrated that the wavelet approach is a viable solution for fault identification under these conditions.

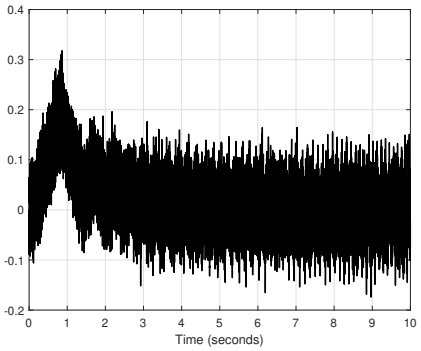
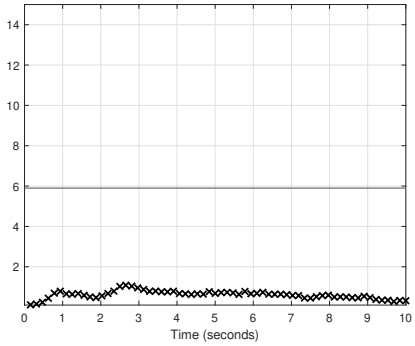
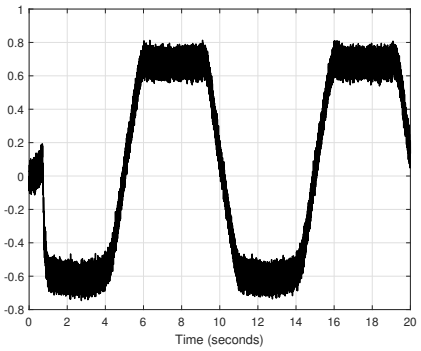
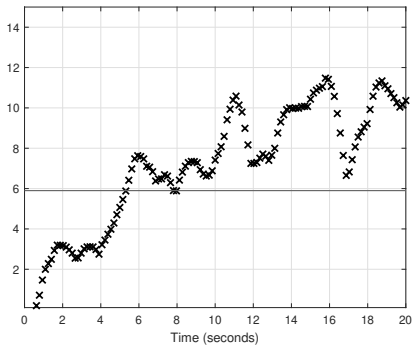
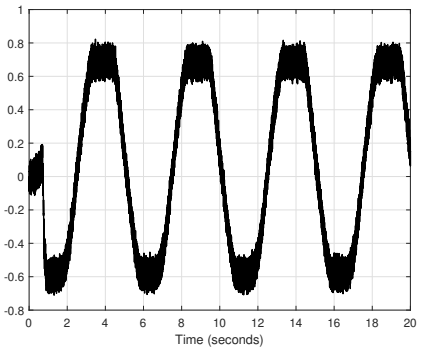
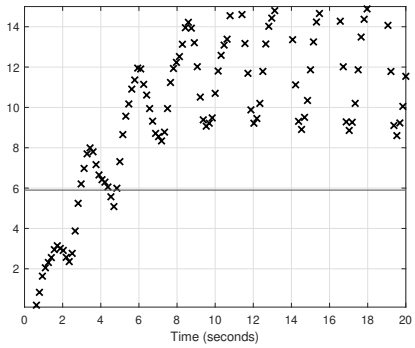
7. Conclusion and Future Work

This article presented a wavelet-based monitor for OFCs located in the piston LVDT of an active-active flight control actuator. The approach combines a closed-loop Luenberger observer, with feedback from the piston position, the servo-valve spool position and the chamber pressure differential, with a DWT residual evaluation layer that uses a Daubechies order-3 mother wavelet, a 256-sample buffer at 6.4 Hz, and split thresholds for the low and high frequency bands.

The simulation results show that the proposed monitor detects both electrical and mechanical liquid LVDT faults in the 0.1 to 2 Hz range within two cycles of fault onset. In the low-frequency band (0.1, 0.2 Hz), the detection margin is wide; in the high-frequency band (0.5, 0.7, 1, 2 Hz), the margin is narrower but still around 100% over the no-fault wavelet coefficient. The DWT layer is also effective in rejecting the high-frequency noise that the pressure sensor introduces into the observer feedback.

The results were obtained under nominal modeling conditions, in continuous time, and without external oscillatory aerodynamic loads. Future work includes a discrete-time implementation aligned with the target sampling rate; robustness assessment under component aging, parameter variations

Table 3 – Residual X_p and wavelet coefficients — low-frequency band.

Fault	Residual X_p (in)	Wavelet coefficients
No fault		
0.1 Hz		
0.2 Hz		

and measurement noise, possibly using a Monte Carlo framework; evaluation against oscillatory aerodynamic loads to characterize false-alarm behavior; extension to solid faults; and a comparative benchmark against other methods, such as oscillation cycle counting on the same residual, to quantify the added value of the wavelet layer.

8. Contact Author E-mail Address

The corresponding author of the present paper can be contacted at the following email address: isa.skusa@gmail.com.

9. Copyright Statement

The authors confirm that they, and/or their company or organization, hold copyright on all of the original material included in this paper. The authors also confirm that they have obtained permission, from the copyright holder of any third party material included in this paper, to publish it as part of their paper. The authors confirm that they give permission, or have obtained permission from the copyright holder of this paper, for the publication and distribution of this paper as part of the ICAS proceedings or as individual off-prints from the proceedings.

References

[1] Efrain Alcorta-Garcia, Ali Zolghadri, and Philippe Goupil. A nonlinear observer-based strategy for aircraft oscillatory failure detection: A380 case study. *IEEE Transactions on Aerospace and Electronic Systems*, 47(4):2792–2806, 2011.

[2] Ali Zolghadri, David Henry, J Cieslak, Denis Ee, and Philippe Goupil. *Fault Diagnosis and Fault-Tolerant Control and Guidance for Aerospace Vehicles Advances in Industrial Control From Theory to Application*. 2014.

[3] P Goupil. Oscillatory failure case detection in the a380 electrical flight control system by analytical redundancy. *IFAC Proceedings Volumes*, 40(7):681–686, 2007.

[4] Loïc Lavigne, Ali Zolghadri, Philippe Goupil, and Pascal Simon. Oscillatory failure case detection for new generation airbus aircraft: a model-based challenge. *Proceedings of the IEEE Conference on Decision and Control*, pages 1249–1254, 2008.

[5] Do Hieu Trinh, Benoît Marx, Philippe Goupil, and José Ragot. Oscillatory failure detection in the flight control system of a civil aircraft using soft sensors. *New Sensors and Processing Chain*, pages 85–105, 2014.

[6] D. Els. Detection of oscillatory actuator failures in passenger airliners, 2019.

[7] M. Forouzanfar, H. Safaeipour, and A. Casavola. Oscillatory failure case detection in flight control systems via wavelets decomposition. *ISA Transactions*, 128:47–53, 9 2022.

[8] Andreas Varga and Daniel Ossmann. Lpv-model based identification approach of oscillatory failure cases. *IFAC Proceedings Volumes*, 45(20):1347–1352, 2012.

[9] Helge Sachs, Udo B Carl, and Frank Thielecke. Monitoring of oscillatory failure cases for the reduction of structural loads in an aeroelastic aircraft. 2008.

[10] Ruqiang Yan, Robert X Gao, and Xuefeng Chen. Wavelets for fault diagnosis of rotary machines: A review with applications. *Signal Processing*, 96:1–15, 2014.

[11] MJ Zuo, J Lin, and X Fan. Feature separation using ica for a one-dimensional time series and its application in fault detection. *Journal of Sound and Vibration*, 287(3):614–624, 2005.

[12] W.X. Yang and X.M. Ren. Detecting impulses in mechanical signals by wavelets. *EURASIP Journal on Applied Signal Processing*, 2004(8):1156–1162, 2004.

[13] J.T. Kim, Y.S. Lee, and C.B. Yun. A comparative study on damage detection of rotor systems. *Journal of Mechanical Science and Technology*, 21(4):624–632, 2007.

[14] C Castejon, JC Garcia-Prada, M Jimenez, and LA Garcia-Escudero. A two-stage neural network approach for fault diagnosis in rolling element bearings using wavelet packet decomposition. *Smart Materials and Structures*, 16(5):1801–1810, 2007.

[15] M. Singh, R.P. Maheshwari, and B.K. Panigrahi. Transmission line fault detection and classification. 2011.

[16] P.S. Addison. *The Illustrated Wavelet Transform Handbook: Introductory Theory and Applications in Science, Engineering, Medicine and Finance, Second Edition*. CRC Press, 2017.

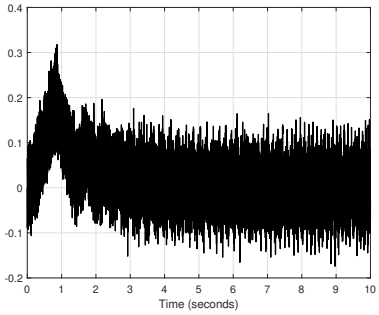
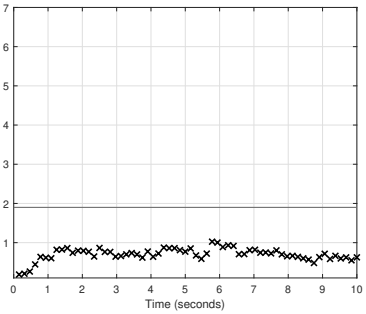
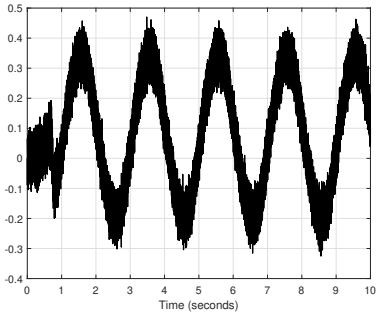
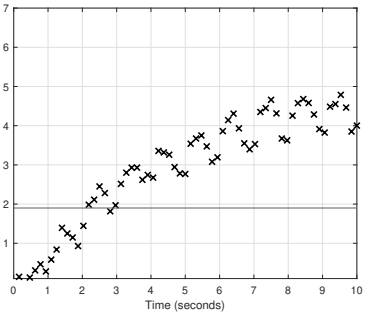
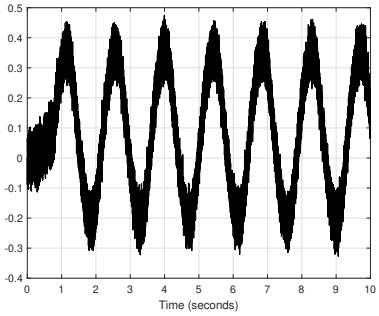
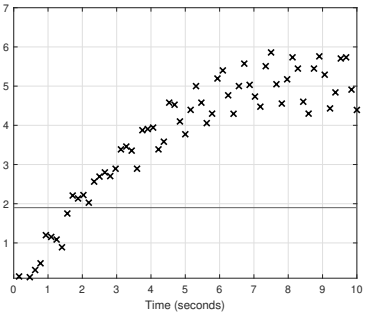
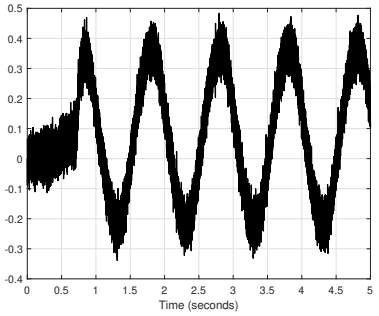
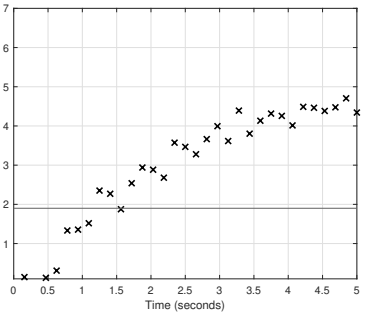
[17] P.s Keogh, Clifford Burrows, and Mehmet Sahinkaya. Adaptive control of rotor vibration using compact wavelets this paper investigates the use of dyadic wavelets for the control of multifrequency rotor.

[18] C. A. Constantino. Hydraulic actuation system modeling: An analysis of high frequency modelling, 2010.

[19] H. M. S. Ballesteros. Dynamic stiffness enhancement of a flight control actuator using control techniques, 2015.

[20] Apinai Rerkratn, Amata Luangpol, Wandee Petchmaneelumka, and Vanchai Riewruja. Position signal detector for linear variable differential transformer. *Energy Reports*, 6:603–607, 2020. 2020 The 7th International Conference on Power and Energy Systems Engineering.

Table 4 – Residual X_p and wavelet coefficients — high-frequency band.

Fault	**Residual X_p (in)**	**Wavelet coefficients**
No fault		
0.5 Hz		
0.7 Hz		
1 Hz		
2 Hz	